IEEE Access
Multidisciplinary | Rapid Review | Open Access Journal

Received March 26, 2021, accepted April 22, 2021, date of publication April 26, 2021, date of current version May 4, 2021.

Digital Object Identifier 10.1109/ACCESS.2021.3075628

Markerless Navigation System for Orthopaedic Knee Surgery: A Proof of Concept Study

XUE HU, HE LIU, AND FERDINANDO RODRIGUEZ Y. BAENA, (Member, IEEE)
Mechatronics in Medicine Laboratory, Imperial College London, London SW7 2AZ, U.K.
Corresponding author: Xue Hu (xue.hu17@imperial.ac.uk)

ABSTRACT Current computer-assisted surgical navigation systems mainly rely on optical markers screwed into the bone for anatomy tracking. The insertion of these percutaneous markers increases operating complexity and causes additional harm to the patient. A markerless tracking and registration algorithm has recently been proposed to avoid anatomical markers for knee surgery. The femur points were directly segmented from the recorded RGBD scene by a neural network and then registered to a pre-scanned femur model for the real-time pose. However, in a practical setup such a method can produce unreliable registration results, especially in rotation. Furthermore, its potential application in surgical navigation has not been demonstrated. In this paper, we first improved markerless registration accuracy by adopting a bounded-ICP (BICP) technique, where an estimate of the remote hip centre, acquired also in a markerless way, was employed to constrain distal femur alignment. Then, a proof-of-concept markerless navigation system was proposed to assist in typical knee drilling tasks. Two example setups for global anchoring were proposed and tested on a phantom leg. Our BICP-based markerless tracking and registration method has better angular accuracy and stability than the original method, bringing our straightforward, less invasive markerless navigation approach one step closer to clinical application. According to user tests, our proposed optically anchored navigation system achieves comparable accuracy with the state-of-the-art (3.64 ± 1.49 mm in position and $2.13\pm0.81^\circ$ in orientation). Conversely, our visually anchored, optical tracker-free setup has a lower accuracy (5.86 ± 1.63 mm in position and $4.18\pm1.44^\circ$ in orientation), but is more cost-effective and flexible in the operating room.

INDEX TERMS Computer-assisted orthopaedic surgery, hip centre measurement, markerless registration, surgical navigation.

I. INTRODUCTION

The potential of Computer Assisted Orthopaedic Surgery (CAOS) to improve the accuracy and efficiency of surgery has been well-proven [1]. The surgical plans are made preoperatively and displayed intraoperatively to surgeons to guide the manual task. CAOS navigation is especially beneficial for those surgical procedures that require a high degree of accuracy and reproducibility [2], [3]. For example, for severe femur osteochondral defects (OCD) that cannot be treated conservatively, repair of the lesion with a synthetic implant is an effective option [4]–[6]. After lesion removal, the implant should be correctly placed into the femur so that the replacement is congruent with the surrounding anatomy; otherwise, mechanical wear may lead to accelerated failure, with clear implications for the patient [7]. Compared to the freehand technique, computer-navigated OCD treatment yields a significantly better clinical outcome [8].

The real-time target pose is essential to dynamically update the plan-contained model so that it can align with the surgical site [9]. The initial bone pose can be obtained in two principal ways. With image-based methods, the anatomical landmarks (e.g., implanted fiducials or surface points) are measured by a surgeon with a tracked probe and registered to a model generated from preoperative images by point-based or surface-based approaches. In image-less methods, the target bone is digitised with a tracked probe so that a generic kinematic and/or morphological model can be parametrised and adapted to it [10]. The resulting static pose needs to be further updated by dynamic target tracking, since the bone inevitably moves during surgery. Optical tracking is the most popular choice because of its high accuracy and compact footprint. A dynamic reference frame (DRF) containing infrared (IR) light-emitting diodes

The associate editor coordinating the review of this manuscript and approving it for publication was Yuan Zhuang.

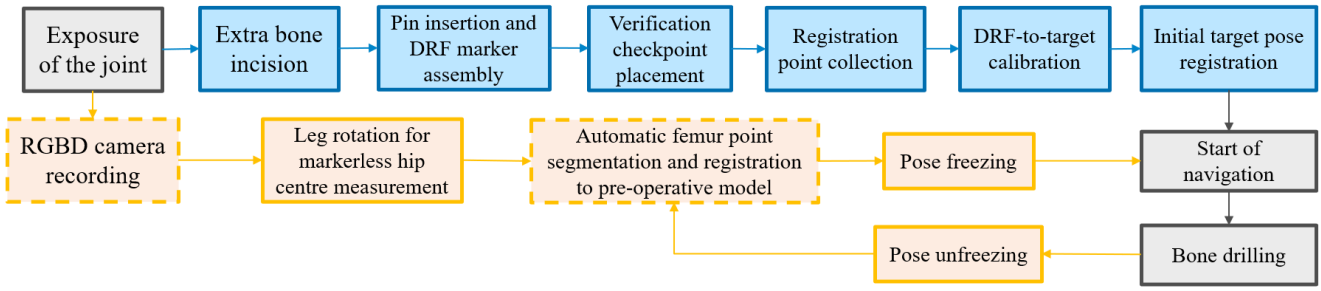

FIGURE 1. Comparison of the conventional marker-based (blue) and the proposed markerless orthopaedic navigation workflows. The processes requiring user manipulation are bordered with solid lines.

(LED) or infrared light-reflecting markers is pinned to the target bone. An additional marker is usually used to verify the rigid DRF insertion. Then, the surgeon collects registration points, according to which the initial bone pose and the rigid DRF-to-bone transformation can be calibrated. During online tracking, the initially-registered bone pose is continuously updated by monitoring the optically tracked DRF movement (Figure 1). Such procedure, however, lends itself to a long workflow [11], possible human-induced errors [12], and most importantly, the additional incisions that may cause infection, nerve injury, and bone fracture for patients [11].

Automatic markerless target tracking and registration are desired to reduce such risks and encourage the broader acceptance of CAOS systems. Markerless tracking and registration algorithm has been proposed in [13], [14] for knee surgeries. A deep neural network was trained to segment the target femur from the RGB-D capture of surgical site. The segmented femur points were then registered to a pre-scanned model of the corresponding limb by the iterative closest point (ICP) method [15], [16] in real-time to obtain the spatial knee pose. The best-reported registration accuracy is 6.66° and 2.74 mm when the target is held static. Such accuracy (especially its angular component) is not acceptable for clinical applications [14]. Furthermore, such markerless technique has not been applied to surgical navigation.

To move the markerless tracking and registration one step closer to surgical viability, in this paper, we first improved the current algorithm by adopting a bounded-ICP (BICP) registration. Then, a markerless navigation system was designed for computer-assisted OCD repair, as an example application to demonstrate the added value of this novel registration and tracking method. Our goal is to align a surgical tool with the planned path in both position and orientation under the visual guidance provided by our navigation system. In addition to the traditional optical tracker-anchored (OTA) setup that requires an external tracker, a more flexible and cost-effective visual marker anchored (VMA) setup was proposed and tested. The navigated femur drilling performance under both setups was evaluated with a small volunteer group on a phantom leg.

To the best of our knowledge, this is the first study on markerless navigation for knee surgery. Compared to the conventional optical marker-based navigation system, our proposed systems are less invasive and more direct in the workflow (Figure 1). Our contributions include:

1) Improved performance of markerless tracking and registration by integrating a BICP registration in the workflow;
2) A proof-of-concept markerless CAOS navigation system to assist in knee surgeries.;
3) Two world anchoring choices (OTA and VMA) for the proposed navigation system;
4) Phantom-based evaluation of navigation performance with user studies;

II. RELATED WORK

A. MARKERLESS FEMUR TRACKING AND REGISTRATION

In orthopaedic surgeries, it is hard to explicitly define clear and robust features as the bone is less geometrically feature-rich and usually exposed within a complex environment surrounded by blood and tissues. Neural networks can be trained to "learn" comprehensive semantics using labelled dataset. A proof-of-concept study was outlined in [14], and a more systematic validation was provided by [13]. Both works used a consumer-level RGB-D camera to record surgical site. Two sequential convolutional neural networks were trained to segment the target anatomy from real-time camera captures automatically. As shown in Figure 2 (he detailed network architecture can be found in [13]), the knee was first localised in the RGB capture by a pre-trained localisation network. According to the inferred region of interest (ROI), the depth frame was cropped to remove the irrelevant background. The cropped frame was passed to a pre-trained segmentation network to predict the possibility that a 3D point belongs to the femur surface. Points with the possibility higher than a threshold (i.e., 80 %) can be regarded as valid femur points. The segmented femur points could be registered to a pre-scanned target model in every frame for the real-time knee pose tracked in the depth camera.

B. BICP REGISTRATION

With the limited spread of measured points caused by the reduced femur exposure, the rotational accuracy of initially-registered target pose quickly degenerates. Unlike

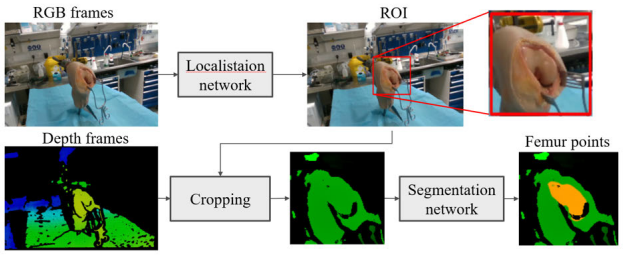

FIGURE 2. Markerless femur tracking using RGBD captures by two pre-trained convolutional neural networks. Figure adapted from [13].

the traditional ICP registration that minimises the distance between corresponding points on the two surfaces, BICP registration, as developed for the commercial Acrobot robotic system [17], uses an additional remote pair of corresponding points (e.g., the hip centre) to bound the registration error for distal points. The forced alignment of remote points reduces the degrees of freedom associated with the convergence process [18], making the iterative registration potentially more stable.

Algorithm 1 Algorithm for BICP Registration

Input: Measured femur points $\{c_i^{(R)}\}$ $(i = 1, 2, \ldots, N)$, measured hip centre $h^{(R)}$, model femur points $\{m_j^{(M)}\}$ $(j = 1, 2, \ldots, M)$ where $M \gg N$, model hip centre $h^{(M)}$;

Output: Transformation T that aligns measurement $\{c_i^{(R)}, h^{(R)}\}$ with model $\{m_j^{(M)}, h^{(M)}\}$;

1: **Initial Transformation:** Global registration between $\{c_i^{(R)}\}$ and $\{m_j^{(M)}\}$.
2: Align two hip centres.
3: **while** iter $\leq$ Maximum iteration **do**
4: Update $c_i^{(R)} = Tc_i^{(R)}$.
5: Search the closest point of $c_i^{(R)}$ in $\{m_j^{(M)}\}$ for $c_i^{(M)}$.
6: Calculate $k^{(R)} = \frac{1}{N}\sum_{i=1}^{N} c_i^{(R)}$, $k^{(M)} = \frac{1}{N}\sum_{i=1}^{N} c_i^{(M)}$.
7: Rotate $\{c_i^{(R)}\}$ around the aligned hip centre so that the measured mechanical axis $h^{(R)}k^{(R)}$ aligns with the model mechanical axis $h^{(M)}k^{(M)}$ after transformation.
8: Further translate the measured femur points along the aligned mechanical axis to minimise the distance between distal femur centres;
9: Further rotate the measured femur points around the aligned mechanical axis to minimise the point-wise angular mismatch between the corresponding femur points;
10: Update T. iter++.
11: **end while**

BICP registration for a femur surface is shown in 1 and Figure 3. In practice, the model containing knee points $\{m_j^{(M)}\}$ and hip joint $h^{(M)}$ could be generated from preoperative images. The distal femur points in robot space $\{c_i^{(R)}\}$ could be measured by probe digitising. The hip centre $h^{(R)}$ can be estimated by functional approaches that use kinematics and geometrical constraints during limb motion [19]. For

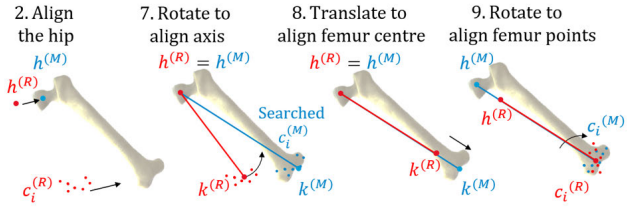

FIGURE 3. Illustration of key steps in BICP registration. The step index corresponds to the 1.

example, $h^{(R)}$ can be modelled as the pivot point around which the leg is rotated. The rotational centre can be obtained by sphere-fitting of the collected landmark positions (e.g., a marker pinned into the distal femur) acquired while the limb is rotated about the hip socket with the pelvis held in place [20].

III. IMPROVEMENT OF MARKERLESS REGISTRATION

Due to the lack of realistic training data, the limited quality of depth camera and the complex surgical scene, the segmented target point cloud is neither clean nor complete [13], [14]. For a noisy point cloud with limited spatial spread, traditional ICP registration becomes inaccurate (especially in orientation) and unstable.

This section aims to improve the accuracy and precision of markerless registration by adopting the BICP method, which is less sensitive to the sampling quality at the distal end. The proposed workflow was simulated on a phantom knee held by a metal leg (Figure 4). The metal leg can rotate around a ball joint (i.e., the hip centre) clamped on the table. The same commercial RGB-D camera (RealSense D415, Intel Corp.) as in [13] was used to track a partially exposed femur surface. The world coordinate was provided by an optical tracker (FusionTrack 500, Atracsys LLC.). Such a system is referred to as "optical tracker anchored" (OTA) in subsequent sections.

A. HIP CENTRE MEASUREMENT

Unlike state-of-the-art that uses additional markers to track the limb motion, the femur surface's origin ($p = [0, 0, 0, 1]^T$) was used as the "landmark" in our setup. The femur pose $F^{(D)}$ was tracked by the same markerless ICP-based registration method in [13] during leg rotation. Since only the origin position (not affected by the registered orientation) was considered in this step, ICP-based tracking was sufficient for hip centre estimation purposes. The "landmark" tracked in the depth camera frame D was then transformed to the static world space W. At a time t, the global landmark position was given by:

$$p^{(W)}(t) = {}^{W}_{M_1}T(t) \times {}^{M_1}_{D}T \times F^{(D)}(t) \times p \tag{1}$$

where M_1 was a DRF rigidly attached to the depth camera (Figure 4). ${}^{W}_{M_1}T$ was the pose of marker M_1 tracked by the optical tracker. The transformation from depth frame to the marker (${}^{M_1}_{D}T$) was a constant matrix that can be calibrated

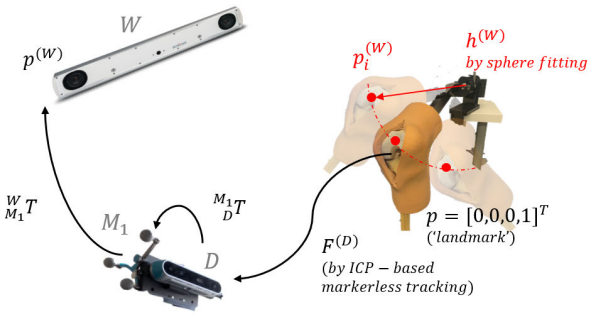

FIGURE 4. Involved transformations during markerless hip centre measurement.

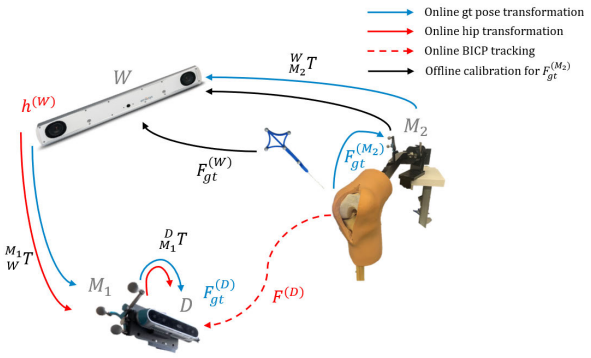

FIGURE 5. Involved transformations for the evaluation of online BICP-based markerless tracking and registration.

once as follows: an asymmetric object S was captured by the depth camera and manually segmented to obtain the point cloud $S^{(D)}$. Without moving the object, the same surface was digitised by a tracked probe to obtain $S^{(W)}$. Two point clouds were then registered to get ${}^{W}_{D}T$. Without moving the depth camera, according to the tracked pose of M_1, we had:

$$ {}^{M_1}_{D}T = {}^{W}_{M_1}T^{-1} \times {}^{W}_{D}T \tag{2} $$

The metal leg was rotated N times around the ball joint. $h^{(W)}$ was fitted from the collected landmark positions $\{p_1^{(W)}, \ldots, p_N^{(W)}\}$ by an 3D version of hyperaccurate algebraic sphere fit algorithm [21]. The algorithm, combining both Pratt and Taubin fit, has no essential bias. More details of our adapted 3D version can be found in Appendix A.

B. BICP REGISTRATION

Before online tracking, the geometry of the femur surface and metal leg was scanned by an HDI Compact 3D Scanner (LMI technologies Inc.) to measure the model femur points $\{m_j^{(M)}\}$ and model hip centre $h^{(M)}$. For online BICP registration, the measured hip centre $h^{(W)}$ was transformed from W to D for $h^{(D)}$. Captured RGB-D images were processed by the pre-trained segmentation networks femur points $\{c_i^{(D)}\}$ (i.e., $\{c_i^{(R)}\}$).

BICP registration was scripted in python and ran on a computer (IntelR©CoreTMi5-8250U processor with 8 gigabytes memory and no graphics processing unit) in real-time. During each iteration, corresponding points were searched by a K-D tree [22], as in [18]. The original BICP method searches measured key points' counterparts in the model space since the manually probed points are fewer than model points. However, in our case, not all ''measured'' points are reliable, and wrongly segmented points may not have correspondences in the pre-scanned femur model. Therefore, we reversed the search direction (i.e., find a sparse femur model's point-wise counterparts within tracked femur points). Perturbations were added during the BICP computation to improve global convergence: The BICP was first run with reduced maximum iterations (e.g., 20). After each run, a random varus-valgus/anterior-posterior rotation (within ±5°) and a random translation along the mechanical axis (within 10 mm) were added to the current transformation estimate. When the registration error decreased to a threshold (e.g., 3 mm), a random axial rotation (within ±5°) was added to the obtained transformation, and the BICP was then allowed to run with the maximum number of iterations (e.g., 800).

TABLE 1. Angular mismatch of the resulting mechanical axis between marker-based and markerless hip centre measurement for OTA system.

	Transverse plane	Coronal plane	Sagittal plane
Angular diff (°)	1.27±0.45	0.54±0.15	0.23±0.13

C. EVALUATION

For the evaluation purpose, an optical marker (labelled M_2) was attached to the metal leg to provide a ground truth (gt) for the evaluation of the measured hip centre. Figure 5 provides the system setup. The constant gt femur pose in M_2 coordinate was calibrated offline according to:

$$ F_{gt}^{(M_2)} = {}^{W}_{M_2}T^{-1} \times F_{gt}^{(W)} \tag{3} $$

where $F_{gt}^{(W)}$ could be obtained by standard femur surface digitising. ${}^{W}_{M_2}T$ was the pose of M_2 optically tracked in world.

1) MEASURED HIP CENTRE

We manually rotated the leg around the clamped hip joint and collected more than 30 positions of M_2 to fit the gt hip centre $h_{gt}^{(W)}$. Figure 6 shows that the markerless and marker-based hip centre measurements have similar accuracy and are both spatially well-defined. The fitted hip centres $h_{gt}^{(W)}$ and $h^{(W)}$ were both transformed to the femur coordinate using the transformed gt femur pose $F_{gt}^{(D)}$. The measurement error was defined as the angular misalignment between the gt and markerless mechanical axis (i.e., the line connecting the femur centre to the measured hip centres $h_{gt}^{(F)}$ and $h^{(F)}$). The pairwise markerless and marker-based hip centre measurement were repeated 10 times. Table 1 shows the quantitative error in 3 anatomical planes (defined by the gt mechanical axis and gross condyles orientation to identify the medial-lateral direction).

2) TIME CONSUMPTION

The time required for markerless tracking and registration at different stages was measured under the current hardware and software conditions. More than 50 frames

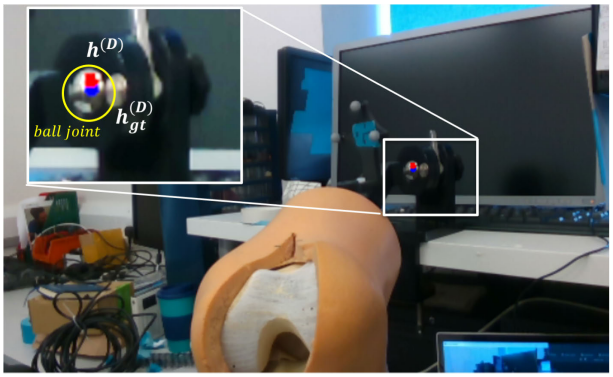

FIGURE 6. Measured $h^{(D)}$ (red) and $h^{(D)}_{gt}$ (blue) transformed in a captured RGB frame.

FIGURE 7. Breakdown of time spent for BICP-based markerless tracking and registration.

TABLE 2. Translational and rotational tracking errors with no leg or camera movement.

	ICP	BICP
3D translational error (mm)	4.57±0.43	4.75±0.27
3D rotational error (°)	6.67±0.53	0.81±0.44
Rotational error in transverse plane (°)	1.10±0.52	0.43±0.66
Rotational error in sagittal plane (°)	3.39±0.99	0.15±0.13
Rotational error in coronal plane (°)	5.55±0.20	0.29±0.30

were recorded. The original ICP-based algorithm updates at approximately 5-6 Hz [13], while the proposed BICP-based algorithm updates at a higher rate of 7-8 Hz. The breakdown of timings at each stage is shown in Figure 7.

3) 3D MARKERLESS REGISTRATION ERROR

The 3D tracking error was defined as the relative transformation from the tracked surface to the gt surface in depth camera coordinates:

$$T_{err}(t) = F^{(D)}_{gt}(t)^{-1} \times F^{(D)}(t) \tag{4}$$

We also implemented the original ICP-based markerless registration used in [13] for comparison. For both methods, in the starting frame, an initial transformation was obtained by random sample consensus (RANSAC) global alignment. In all subsequent frames, the current transformation is used as the next estimate to achieve iterative refinement. We tested the registration accuracy during static tracking (i.e., both camera and limb were still) and dynamic tracking (i.e., either camera or limb was moving). Results were shown in Table 2 and Table 3, with the box-and-whisker plots in Figure 8 and Figure 9.

a: ROTATIONAL ERROR

In comparison to the ICP registration, the BICP method significantly reduces the level of rotational misalignment (p-values<0.001, by student t-tests) under either

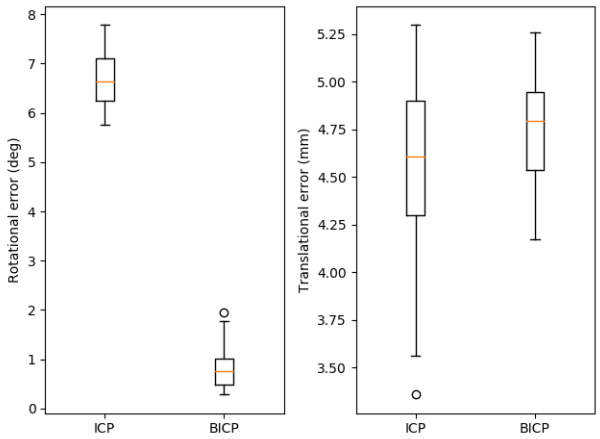

FIGURE 8. Box-and-whisker plots of the absolute tracking errors in orientation and position with no leg or camera movement. The box extends from the median to the 25% – 75% range of the data spread. The whiskers extend to the most extreme inliers (≈ $\pm 2.7\sigma$ and 99.3% coverage for a normally distributed dataset).

TABLE 3. Translational and rotational tracking errors with dynamic camera or leg movement.

	ICP	BICP
3D translational error (mm)	8.61±3.41	6.76±2.11
3D rotational error (°)	8.42±2.49	1.95±1.61
Rotational error in transverse plane (°)	0.03±1.52	1.03±2.12
Rotational error in sagittal plane (°)	6.72±3.55	0.33±0.44
Rotational error in coronal plane (°)	2.38±3.36	0.11±0.73

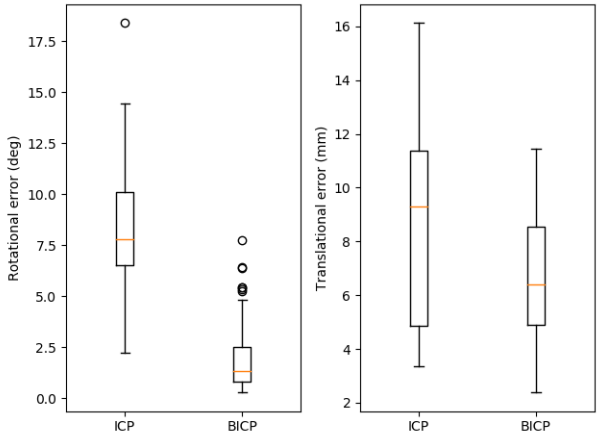

FIGURE 9. Box-and-whisker plots of the absolute tracking errors in orientation and position with dynamic camera or leg movement.

static or dynamic tracking. For all the t-tests mentioned in this paper, data normality was confirmed by D'Agostino and Pearson's test [23], [24]). The transverse alignment is the least accurate for BICP registration but the most accurate for ICP registration. The difference is because, for the BICP method, the rotation in the coronal and sagittal planes is restricted by the remote hip centre while transverse alignment is not. By contrast, for ICP, the rotation in the coronal and sagittal planes is less constrained due to the smaller point spread and lack of features in the condyles than the transverse plane. It is worthwhile mentioning that, according to Table 1, the fact

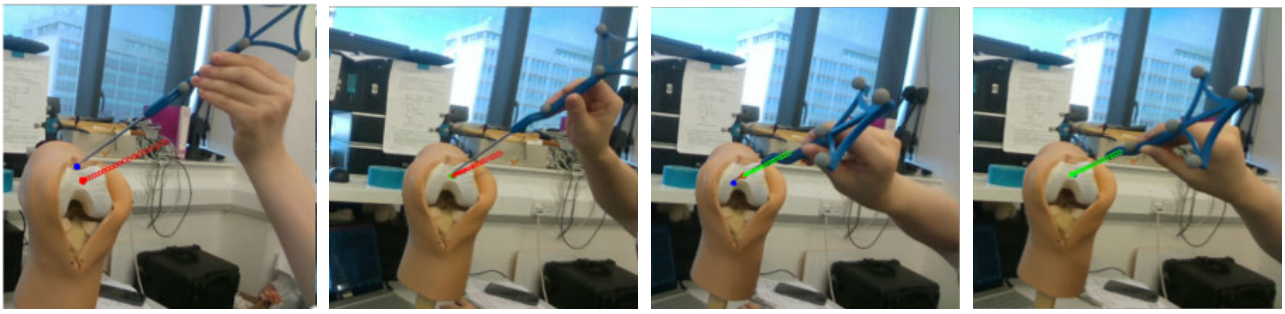

(a) Wrong position and direction (b) Correct position, wrong direction (c) Correct direction, wrong position (d) Correct position and direction

FIGURE 10. Visual guidance displayed on a monitor to navigate the femur drilling in planned pose.

that the hip centre measurement error is most extensive in the transverse plane may also contribute to the highest BICP misalignment in the transverse plane.

b: POSITIONAL ERROR

Regarding the mean, the difference in averaged positional misalignment is not statistically significant (p-value = 0.08 by a student t-test) under static tracking, whereas the error is slightly reduced by BICP (p-value$<$ 0.01) under dynamic tracking. Regarding the variance, BICP improves the system's stability under both dynamic and static modes (standard deviation from 0.43 to 0.27 under static tracking and from 3.413 to 2.11 under static tracking).

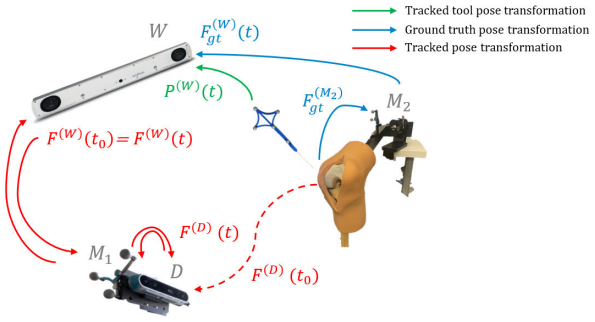

FIGURE 11. Transformation for the evaluation of visual-guided navigation system with "freezing" technique.

IV. MARKERLESS NAVIGATION SYSTEM FOR FEMUR DRILLING

Following the validation of tracking accuracy, we designed a BICP-based markerless navigating system to assist in implant placement, to prove the concept of improved assistance in bone resection. The planned drilling path was displayed as RGB visual clues overlaid on the captured real-time scene on a monitor (Figure 10). Surgeons could refer to the computer-generated information to place the drill guide in the desired position and orientation.

A. SYSTEM DESIGN

Due to the partial occlusion of target surface by the surgical tool and hand during drilling, segmentation may be poor (i.e., it may be incomplete and incorrectly identify femur points within the scene) or even fail. Therefore, dynamic tracking can be unreliable. To maintain stable visual guidance during the operation, we proposed a "freezing" technique. As shown in the red path of Figure 11, at an arbitrary moment t_0, the user can freeze a frame of the dynamically tracked pose after adjusting and securing the limb to the desired pose. The tracked pose was transformed into the static world fame as $F^{(W)}(t_0)$ and used as a reference for subsequent frozen frames. While the pose was frozen, the limb should be kept stationary when possible, but the camera was free to move. The stored global pose was then transformed back to D based on the tracked pose of M_1 for $F^{(D)}(t)$. The user can freely switch between the dynamic tracking mode and frozen navigating mode at any time, in a fast and effortless way. More specifically, in our implementation, the drilling probe with attached markers was used as a switch. If the probe is rotated so that markers can no longer be tracked, the femur will be dynamically tracked. If the probe is rotated so that the attached markers become visible to the camera, the system will progress using a freshly-frozen pose.

During navigation, a virtual vector consisting a head sphere and a body axis (default in red) was overlaid on the captured RGB scene according to the planned path and registered femur pose. A blue dot was rendered on the tracked probe tip. Users should align the probe tip with the displayed plan head sphere, and the observed probe axis with the displayed plan body axis. To assist the rotational alignment, we adopted a colour feedback mechanism that can indicate the correctness of alignment. The system-evaluated error used to change the plan colour was defined as the difference between the tracked probe pose $P^{(W)}$ and the designed entry path transformed into the world frame $P_{plan}^{(W)}$. If the positional and/or orientation difference is less than a threshold (set to 5 mm and 3° in our implementation), the head and/or body of the displayed virtual vector will independently change to green (Figure 11).

B. SYSTEM EVALUATION

The effect of freezing on BICP tracking accuracy was first tested (Figure 12). The tracked femur pose was frozen at the

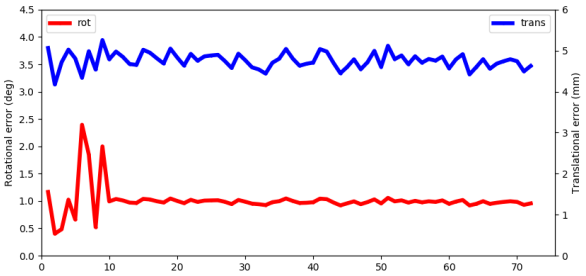

FIGURE 12. Variation of absolute BICP-based markerless registration errors due to pose freezing under OTA setup.

frame 10. After freezing, the camera was dynamically moved to several positions around the target leg. Such procedure was repeated 20 times. According to t-tests, the tracking error level was not noticeably different (rotational error: p-value $= 0.07$; translational error: p-value $= 0.85$), but the rotational variance was reduced from 0.65 to 0.033 and the translational variance was reduced from 0.31 to 0.15. We hypothesise that, since M_1 was accurately tracked by the world-anchored optical tracker, ''freezing'' did not reduce the tracking quality.

Then, two sets of user studies were carried out to test the navigation system's performance in assisting femur drilling. The first set of studies, consisting of two trials, was carried out by the lead author to test the system's repeatability. For each trial, the navigation procedure started with the phantom leg positioned at nine poses (left, right, middle, up, down, upper-left, upper-right, lower-left and lower-right) relative to the depth camera, after which the planned path was displayed to and aligned by the author. The second set of experiments was performed by ten volunteers recruited within the university, who had no prior experience in similar navigation tasks (ethical approval obtained from the Science Engineering Technology Research Ethics Committee, Imperial College London. SETREC number: 20IC6323). They were first instructed to measure the hip centre using the markerless method offline. Then, the ''dynamic tracking-freezing-drilling'' navigation procedure was explained to them. Users can control the procedure with the provided tool, and adjust the leg pose if necessary. When the visual guidance indicated correct alignment (i.e., the colour turned to green) in both position and orientation, users can further adjust the tool for the best virtual-to-real overlay (i.e., final drilling pose). Such navigation was repeated two times by each user.

The actual navigation error was defined as the difference between the final probe insertion location and orientation contained in $P^{(W)}$ and the planned entry path $F_{gt}^{(W)}$ (i.e., transformed by the blue path in Figure 11). The absolute navigation errors and the time taken to align the tool (measured from the display of planned path to final alignment), were recorded in Table 4.

According to the correlation computed between two recorded sequences of navigation errors by author, test-retest reliability was good in translation (coefficient $= 0.81$) and acceptable in rotation (coefficient $= 0.73$) [26]. The overall drilling error is 3.35 mm in position and 2.09° in orientation.

TABLE 4. Navigation errors in position, orientation and alignment time (OTA setup).

	Author	Users	Overall
3D translational error (mm)	3.29±1.23	4.14±1.68	3.64±1.49
3D rotational error (°)	1.96±0.74	2.37±0.85	2.13±0.81
Alignment time (s)	14.76±6.83	28.42±11.31	-

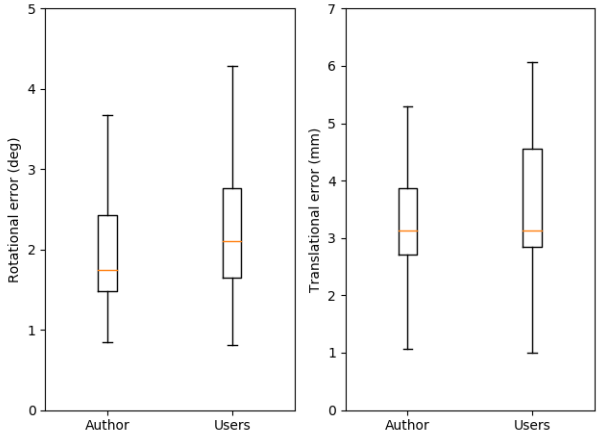

FIGURE 13. Box-and-whisker plots of the absolute navigation errors in position and orientation, assisted by the BICP-based markerless OTA navigation.

According to a t-test between the author group and volunteer group, there is no significant difference in the translational (p-value $= 0.06$) and rotational errors p-value $= 0.09$) obtained, but there is a significant difference in alignment time (p-value<0.001). Such results indicate good usability but a significant learning curve.

V. WORLD ANCHORING BY VISUAL MARKERS

The world anchoring is essential for BICP markerless navigation. Despite their high accuracy, optical tracking systems suffer from a high capital investment cost, and the need to preserve lines-of-sight [27]. Therefore, we propose an alternative ''visual marker anchored'' (VMA) system that uses inexpensive 3D visual markers as the stationary world anchor (noted by W'). Instead of relying on the unique properties of IR tracking markers, the target's natural features (e.g., colour, contours, geometry and depth) that are visually perceivable by the human eye are recorded by a consumer-level RGB-D camera, to depict the target pose relative to the camera. The camera D can be self-localised in W' by the ''inside-out'' tracking of W'. In practice, such a visual anchor should be clamped close to the target anatomy on the surgical bed to ensure the natural visibility during surgery.

A. VISUAL ANCHORING PROCESS

For our VMA setup, we exploited the RGB-D sensing of a multi-marker 3D anchor, to overcome the limitation of RGB sensing in recovering the depth information from the relative size change. As shown in Figure 14, a set of ArUco markers [28] with different IDs were printed on a 3D dodecahedron. ArUco markers were first captured by the RGB frame of the

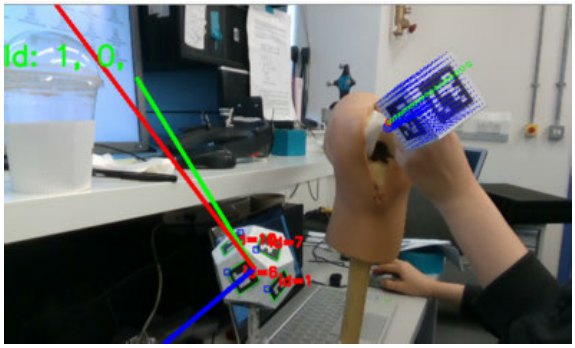

FIGURE 14. Setup of the VMA navigation for a femur drilling task.

TABLE 5. Angular mismatch of the resulting mechanical axis between marker-based and markerless hip centre measurement for VMA system.

	Transverse plane	Coronal plane	Sagittal plane
Angular diff (°)	3.66±1.32	1.43±0.47	0.54±0.39

depth camera and uniquely identified by the OpenCV library [29]. If at least two markers were detected at the same time, the pose of the anchor ${}^{D}_{W'}T_{RGB}$ was optimised from all detected markers by the perspective-n-point (PnP) method. The depth frame was cropped using the estimated ${}^{D}_{W'}T_{RGB}$, according to which a point cloud was generated and registered to a dodecahedron model by ICP with ${}^{D}_{W'}T_{RGB}$ used as the initial pose estimation. The point cloud registration gave the tracked final pose ${}^{D}_{W'}T$.

B. MEASUREMENT AND EVALUATION

1) HIP CENTRE MEASUREMENT

All tracked "landmark" positions were transformed to W' and solved there by the previously mentioned hyperaccurate algebraic sphere-fitting. The camera can move during leg rotation, provided the anchored marker W' remains in the field of view. The gt hip centre for comparison was calculated in the same way but transformed from W to W':

$$h_{gt}^{(W')} = {}^{W'}_{D}T \times {}^{D}_{M_1}T \times {}^{M_1}_{W}T \times h_{gt}^{(W)} \tag{5}$$

The pairwise measurement of $h_{gt}^{(W')}$ and $h^{(W')}$ were also repeated 10 times. As shown in Table 5, the error of markerless hip centre measurements for VMA system is higher (≈ 3-times) than the OTA system (as in Table 1).

2) BICP REGISTRATION

For online BICP registration, the offline measured hip centre $h^{(W')}$ was transformed into D according to the tracked anchor pose ${}^{D}_{W'}T$.

The tracking accuracy was evaluated in the same way as described earlier. As shown in Figure 15, under static conditions, BICP still achieves better accuracy in orientation and less variance in both position and orientation compared to original ICP-based tracking. However, the level of tracking errors obtained by the VMA system (BICP: 2.87±0.47°, 6.61±0.30 mm) is significantly higher compared to the OTA system (BICP: mean 0.81±0.44°, 4.75±0.27 mm) according to a t-test (p-value<0.001).

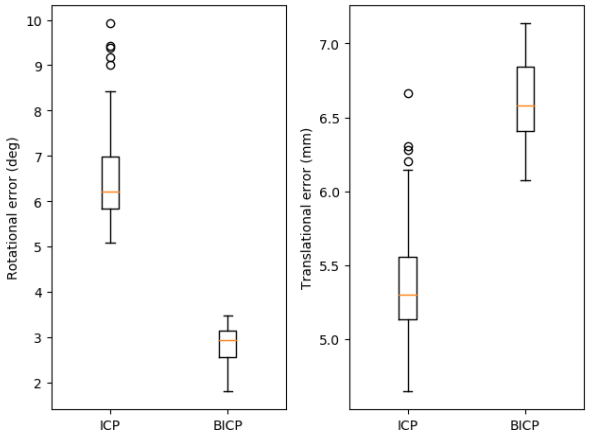

FIGURE 15. Box-and-whisker plots of the static rotational and translational tracking errors obtained by VMA system.

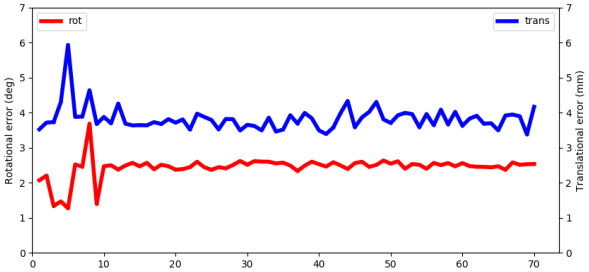

FIGURE 16. Variation of absolute BICP-based markerless registration errors due to pose freezing under VMA setup.

3) MARKERLESS NAVIGATION FOR FEMUR DRILLING

The 3D-printed drilling probe contains a cube with ArUco markers attached on three surfaces (Figure 14). The same "dynamic tracking-freezing-drilling" procedure was adopted to display planned path during hand manipulation.

Figure 16 shows the effect of pose freezing on BICP tracking accuracy under VMA setup. After freezing at the frame 10, the level of tracking error was still not significantly affected (rotational error: p-value = 0.74; translational error: p-value = 0.17, by a t-test), and the variances were reduced (rotational variance from 1.34 to 0.073, translational variance from 0.55 to 0.21).

The user tests were carried out in the same way to assess the navigation performance under VMA setup. According to the computed correlation between the two recorded sequences of drilling errors obtained in the author group, test-retest reliability is acceptable in translation (coefficient = 0.71), but questionable in rotation (coefficient = 0.64) [26]. As shown in Table 6, the average drilling errors are 6.69 mm in position and 4.46° in orientation. According to a t-test performed between the two groups, the p-value is 0.65 in rotation and 0.17 in translation, indicating an insignificant difference in terms of the level of experience. The difference in alignment time is still significant (p-value<0.001). The performance between OTA and VMA systems is significantly different regarding both accuracy and alignment time (p-values<0.05 by t-test).

TABLE 6. Femur drilling errors in position, orientation and alignment time (VMA setup).

	Author	Users	Overall
3D translational error (mm)	6.25±1.35	5.51±1.78	5.86±1.63
3D rotational error (°)	4.29±1.25	4.08±1.58	4.18±1.44
Alignment time (s)	23.45±8.71	71.56±39.23	-

VI. DISCUSSION

A. COMPARISON WITH STATE-OF-THE-ART

The BICP method can effectively improve registration accuracy and stability by bounding the misalignment at the distal femur within the hip centre estimation error. Compared to the original ICP-based tracking method [13], despite a slightly longer workflow and an additional world anchor required for the transformation of the hip centre, BICP-based markerless registration achieves more accurate rotational alignment (static: 0.81°, dynamic: 1.95°), similar positional alignment, and higher precision. According to our user trial, manual femur drilling assisted by the proposed navigation system achieves an average entry pose error of 2.13° and 3.64 mm under the OTA setup and 4.18° and 5.86 mm under the VMA setup.

Regarding navigation accuracy, as shown in Table 7, both our OTA and VMA systems are more accurate than a pilot markerless navigation study for percutaneous needle insertion [30]. Compared to some marker-based state-of-the-art navigation systems, our OTA setup can achieve a similar level of error. Our markerless navigation systems are less invasive and cumbersome in workflow due to the complete removal of anatomical markers. In our implementation, the leg marker was only used for performance evaluation and is not needed for our methods to work as intended. Although artificial markers (e.g., M_1) are still needed for camera localisation and tool tracking, they do not cause any harm to the patient, and the required calibration can be performed beforehand, independently of the patient or intraoperative workflow.

B. OPTICAL TRACKER-FREE NAVIGATION SETUP

Our proposed VMA setup is optical tracker-free, resulting in a potential reduction in the cost of manufacture of surgical navigation system. The offline calibration for ${}^{M_1}_{D}T$ can be avoided. Furthermore, the visual anchor W' allows better operating room (OR) utilisation: in OTA systems, both D and P must be within the line-of-sight of a stationary optical tracker, which constrains the OR layout and consequently, the surgeon's movements. By contrast, in VMA systems, the world frame W' can be passively tracked by a portable camera D. If D is mounted on the surgeon's head, the line-of-sight between D and W' or P will follow on naturally from the surgeon having to keep the patient in their sight during surgery.

However, the VMA system is still less accurate than the OTA system in relation to the hip centre measurement, tracking and guided femur drilling. The lower accuracy could be explained by the limited accuracy and spatial resolution of the current depth camera. The isually tracked noisy tool pose results in an unstable system-evaluated navigation error and unstable colour feedback. Under the same selected acceptance threshold, it takes a significantly longer time for users to achieve stable alignment under the VMA-based setup (Table 6).

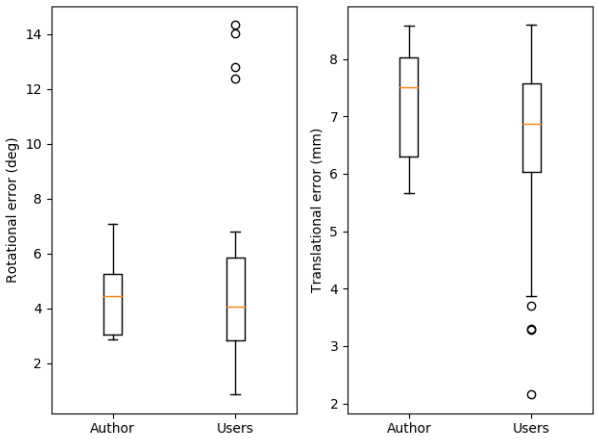

FIGURE 17. Box-and-whisker plots of the absolute drilling errors in position and orientation, assisted by the BICP-based markerless VMA navigation.

C. LIMITATION AND FUTURE WORK

This proof-of-concept demonstration has its own limitations. First, the Realsense D415 camera is a low-accuracy camera not designed for medical applications. The camera quality restricts the accuracy of markerless target registration and visual W' or P tracking. A more advanced RGB-D camera would be essential to improve markerless navigation performance under either the OTA or VMA setup. Several aspects have to be considered for camera selection: the accuracy, precision and spatial resolution of depth-sensing should be high to ensure system reliability; the frame acquisition speed should be comparable to that of optical tracking systems to ensure fast enough tracking updates; the weight and size should be portable to ensure flexibility in OR; and no visible light or patterns should be involved in depth-sensing to ensure the surgical scene is not compromised. In the future, we will collect new datasets and retrain the networks with better cameras, such as the Acusense (Revopoint 3D Technologies Inc.), as to further improve the results of the proposed markerless navigation method.

Second, as the current navigation system displays both real and virtual contents in 2D, the spatial tool alignment requires depth testing [33] that could be time-consuming for an inexperienced user. This explains the significant difference in alignment time measured for author group compared to the volunteer group. To shorten the learning curve and avoid any distractions that could raise a safety concern, a more egocentric head-mounted augmented reality visualisation method should be explored in the future. For example, using an optical see-through (OST) stereo-display, the planned surgical path could be perceived as a 3D vector in front of the user's

TABLE 7. Comparison with state-of-the-art monitor-based surgical navigation systems.

Studies	Application	Anatomical marker used?	Positional error (mm)	Rotational error (°)
Ours (OTA)	Femur drilling for OCD repair	No	3.64±1.49	2.13±0.81
Ours (VMA)			5.86±1.63	4.18±1.44
Seitel et al. [29]	Percutaneous needle insertion	No	6.9 median with (5.9, 8.9) interquartile range	-
Sato et al. [30]	Hip cup placement	Yes, optical markers	3.31±1.08	3.35±1.51
Fotouhi et al. [31] (direct anterior)	Hip cup placement	Yes, visual marker	<3	6.52±5.97 in abduction 1.82±1.89 in anteversion

eyes, as we did in another previous work [34]. The 3D-3D real-to-virtual alignment is more intuitive than the 3D-2D alignment method used here, and surgeons can refer to the displayed information without shifting the eyesight away from the limb.

As a worth-investing option, the accuracy of VMA setup needs to be improved in the future. To name a few possible solutions, better marker libraries (e.g., ALVAR [35]) could be used to improve the speed and accuracy of marker detection, a multi-anchor setup could be used to improve the visual tracking accuracy [27], and a marker-based simultaneous localisation and mapping (SLAM) algorithm [36] could be used to eliminate the restriction that a single anchor must be kept in view at all times.

Finally, current online navigation is not capable of dynamic tracking so that the pose freezing must be used to improve stability under partial target occlusion. Despite the promising result, fully dynamic tracking is desired in practice since the limb is hard to remain still during the intervention. The markerless tracking algorithm should be improved, for example, by network retraining with partially occluded data, target completion by machine learning networks [36], or multi-sensor fusion [37].

VII. CONCLUSION

This paper improves upon a state-of-the-art automatic markerless tracking and registration method by adopting a BICP registration technique to localise the distal femur. In doing so, the angular alignment of femoral components is significantly reduced, moving the markerless method one step closer to clinical application. In the context of a prototypical markerless navigation system to assist in lesion removal for OCD repair, a traditional optical tracker anchored (OTA) setup is proposed, alongside a more cost-effective, visual marker anchored alternative (VMA). The tracking accuracy and navigation accuracy under both setups are assessed in phantom-based experiments, with results demonstrating the effectiveness of our methods. Although these novel approaches do not yet outperform current navigation systems in terms of accuracy, they avoid the need for marker preparation and insertion for online limb tracking, thereby significantly simplifying the surgical workflow, reducing the risk of additional harm for patients, and minimising human-induced errors.

REFERENCES

[1] L. Jud, J. Fotouhi, O. Andronic, A. Aichmair, G. Osgood, N. Navab, and M. Farshad, "Applicability of augmented reality in orthopedic surgery—A systematic review," *BMC Musculoskeletal Disorders*, vol. 21, no. 1, pp. 1–13, Dec. 2020.

[2] W. Siebert, S. Mai, R. Kober, and P. F. Heeckt, "Technique and first clinical results of robot-assisted total knee replacement," *Knee*, vol. 9, no. 3, pp. 173–180, Sep. 2002.

[3] M. A. Conditt and M. W. Roche, "Minimally invasive robotic-arm-guided unicompartmental knee arthroplasty," *J. Bone Joint Surgery*, vol. 91, no. 1, pp. 63–68, 2009.

[4] F. Tatti, H. Iqbal, B. Jaramaz, and F. R. Y. Baena, "A novel computer-assisted workflow for treatment of osteochondral lesions in the knee," *EPiC Ser. Health Sci.*, vol. 4, pp. 250–253, 2020.

[5] P. Bollars, M. Bosquet, B. Vandekerckhove, F. Hardeman, and J. Bellemans, "Prosthetic inlay resurfacing for the treatment of focal, full thickness cartilage defects of the femoral condyle: A bridge between biologics and conventional arthroplasty," *Knee Surg., Sports Traumatol., Arthroscopy*, vol. 20, no. 9, pp. 1753–1759, Sep. 2012.

[6] A. Fuchs, H. Eberbach, K. Izadpanah, G. Bode, N. P. Südkamp, and M. J. Feucht, "Focal metallic inlay resurfacing prosthesis for the treatment of localized cartilage defects of the femoral condyles: A systematic review of clinical studies," *Knee Surg., Sports Traumatology, Arthroscopy*, vol. 26, no. 9, pp. 2722–2732, Sep. 2018.

[7] Y.-W. Moon, C.-W. Ha, K.-H. Do, C.-Y. Kim, J.-H. Han, S.-E. Na, C.-H. Lee, J.-G. Kim, and Y.-S. Park, "Comparison of robot-assisted and conventional total knee arthroplasty: A controlled cadaver study using multiparameter quantitative three-dimensional CT assessment of alignment," *Comput. Aided Surg.*, vol. 17, no. 2, pp. 86–95, Mar. 2012.

[8] P. Di Benedetto, M. Citak, D. Kendoff, P. F. O'Loughlin, E. M. Suero, A. D. Pearle, and D. Koulalis, "Arthroscopic mosaicplasty for osteochondral lesions of the knee: Computer-assisted navigation versus free-hand technique," *Arthroscopy: J. Arthroscopic Rel. Surg.*, vol. 28, no. 9, pp. 1290–1296, Sep. 2012.

[9] C. L. Allen, G. J. Hooper, B. J. Oram, and J. E. Wells, "Does computer-assisted total knee arthroplasty improve the overall component position and patient function?" *Int. Orthopaedics*, vol. 38, no. 2, pp. 251–257, 2014.

[10] K. Radermacher and M. Tingart, "Computer-assisted orthopedic surgery," *Biomedizinische Technik/Biomed. Eng.*, vol. 57, no. 4, pp. 442–448, Jan. 2012.

[11] D. C. Beringer, J. J. Patel, and K. J. Bozic, "An overview of economic issues in computer-assisted total joint arthroplasty," *Clin. Orthopaedics Rel. Res.*, vol. 463, pp. 26–30, Oct. 2007.

[12] A. P. Schulz, K. Seide, C. Queitsch, A. von Haugwitz, J. Meiners, B. Kienast, M. Tarabolsi, M. Kammal, and C. Jàrgens, "Results of total hip replacement using the robodoc surgical assistant system: Clinical outcome and evaluation of complications for 97 procedures," *Int. J. Med. Robot. Comput. Assist. Surg.*, vol. 3, no. 4, pp. 301–306, Dec. 2007.

[13] H. Liu and F. R. Y. Baena, "Automatic markerless registration and tracking of the bone for computer-assisted orthopaedic surgery," *IEEE Access*, vol. 8, pp. 42010–42020, 2020.

[14] P. Rodrigues, M. Antunes, C. Raposo, P. Marques, F. Fonseca, and J. P. Barreto, "Deep segmentation leverages geometric pose estimation in computer-aided total knee arthroplasty," *Healthcare Technol. Lett.*, vol. 6, no. 6, pp. 226–230, Dec. 2019.

[15] Y. Chen and G. Medioni, "Object modeling by registration of multiple range images," *Image Vis. Comput.*, vol. 10, no. 3, pp. 145–155, 1992.

[16] P. J. Besl and N. D. McKay, "Method for registration of 3-D shapes," *Proc. SPIE*, vol. 1611, pp. 586–606, Apr. 1992.

[17] M. Jakopec, S. J. Harris, F. Rodriguez y Baena, P. Gomes, J. Cobb, and B. L. Davies, "The first clinical application of a 'hands-on' robotic knee surgery system," *Comput. Aided Surg.*, vol. 6, no. 6, pp. 329–339, Jan. 2001.

[18] F. Rodriguez y Baena, T. Hawke, and M. Jakopec, "A bounded iterative closest point method for minimally invasive registration of the femur," *Proc. Inst. Mech. Eng., H, J. Eng. Med.*, vol. 227, no. 10, pp. 1135–1144, Oct. 2013.

[19] H. Kainz, C. P. Carty, L. Modenese, R. N. Boyd, and D. G. Lloyd, "Estimation of the hip joint centre in human motion analysis: A systematic review," *Clin. Biomech.*, vol. 30, no. 4, pp. 319–329, May 2015.
[20] F. R. Y. Baena and B. Davies, "Robotic surgery: From autonomous systems to intelligent tools," *Robotica*, vol. 28, no. 2, p. 163, 2010.
[21] A. Al-Sharadqah and N. Chernov, "Error analysis for circle fitting algorithms," *Electron. J. Statist.*, vol. 3, no. none, pp. 886–911, Jan. 2009.
[22] J. L. Bentley, "Multidimensional binary search trees used for associative searching," *Commun. ACM*, vol. 18, no. 9, pp. 509–517, Sep. 1975.
[23] R. B. D'Agostino, "An omnibus test of normality for moderate and large size samples," *Biometrika*, vol. 58, no. 2, pp. 341–348, 1971.
[24] R. D'Agostino and E. S. Pearson, "Tests for departure from normality. Empirical results for the distributions of b^2 and $\sqrt{b}^1$," *Biometrika*, vol. 60, pp. 613–622, Dec. 1973.
[25] D. George, *SPSS for Windows Step by Step: A Simple Study Guide and Reference, 17.0 Update, 10/E*. London, U.K.: Pearson, 2011.
[26] R. Simoes, C. Raposo, J. P. Barreto, P. Edwards, and D. Stoyanov, "Visual tracking vs optical tracking in computer-assisted intervention," Inst. Syst. Robot., Univ. Coimbra, Coimbra, Portugal, Tech. Rep. [tmi2018], 2019. [Online]. Available: https://home.deec.uc.pt/~jpbar/visarthro/Materials/tmi2018.pdf
[27] S. Garrido-Jurado, R. Muñoz-Salinas, F. J. Madrid-Cuevas, and M. J. Marín-Jiménez, "Automatic generation and detection of highly reliable fiducial markers under occlusion," *Pattern Recognit.*, vol. 47, no. 6, pp. 2280–2292, 2014.
[28] Itseez. (2015). *Open Source Computer Vision Library*. [Online]. Available: https://github.com/itseez/opencv
[29] A. Seitel, N. Bellemann, M. Hafezi, A. M. Franz, M. Servatius, A. Saffari, T. Kilgus, H.-P. Schlemmer, A. Mehrabi, and B. A. Radeleff, "Towards markerless navigation for percutaneous needle insertions," *Int. J. Comput. Assist. Radiol. Surg.*, vol. 11, no. 1, pp. 107–117, 2016.
[30] Y. Sato, T. Sasama, N. Sugano, K. Nakahodo, T. Nishii, K. Ozono, K. Yonenobu, T. Ochi, and S. Tamura, "Intraoperative simulation and planning using a combined acetabular and femoral (CAF) navigation system for total hip replacement," in *Proc. Int. Conf. Med. Image Comput. Comput.-Assist. Intervent.* Berlin, Germany: Springer, 2000, pp. 1114–1125.
[31] J. Fotouhi, C. P. Alexander, M. Unberath, G. Taylor, S. C. Lee, B. Fuerst, A. Johnson, G. M. Osgood, R. H. Taylor, and H. Khanuja, "Plan in 2-D, execute in 3-D: An augmented reality solution for cup placement in total hip arthroplasty," *J. Med. Imag.*, vol. 5, no. 2, 2018, Art. no. 021205.
[32] W.-Y. Chan and P.-A. Heng, "Visualization of needle access pathway and a five-DoF evaluation," *IEEE J. Biomed. Health Inform.*, vol. 18, no. 2, pp. 643–653, Oct. 2013.
[33] H. Liu, E. Auvinet, J. Giles, and F. Rodriguez y Baena, "Augmented reality based navigation for computer assisted hip resurfacing: A proof of concept study," *Ann. Biomed. Eng.*, vol. 46, no. 10, pp. 1595–1605, Oct. 2018.
[34] K. Rainio and A. Boyer, "ALVAR–a library for virtual and augmented reality user's manual," VTT Augmented Reality Team, Helsinki, Finland, Tech. Rep. [v.2.0], 2013. [Online]. Available: http://virtual.vtt.fi/virtual/proj2/multimedia_old/ALVAR_v2_User_Manual.pdf
[35] A. J. Davison, "Real-time simultaneous localisation and mapping with a single camera," in *Proc. IEEE Int. Conf. Comput. Vis.*, Oct. 2003, p. 1403.
[36] O. Wiles and A. Zisserman, "SilNet : Single- and multi-view reconstruction by learning from silhouettes," 2017, *arXiv:1711.07888*. [Online]. Available: http://arxiv.org/abs/1711.07888
[37] C. He and Y. Liu, "Inertial and optical sensor fusion to compensate for partial occlusions in surgical tracking systems," in *Proc. Int. Conf. Opt. Instrum. Technol., Opt. Syst. Modern Optoelectron. Instrum.*, Aug. 2015, Art. no. 961802.

XUE HU received the B.Eng. degree in aircraft propulsion from Beihang University (BUAA), Beijing, China, in 2017, and the M.Sc. degree in advanced mechanical engineering from Imperial College London, U.K., in 2018. She is currently pursuing the Ph.D. degree with the Mechatronics in Medicine Laboratory, Department of Mechanical Engineering, Imperial College London. Her research interests include augmented reality, computer-assisted orthopaedic surgery, and machine-vision applications.

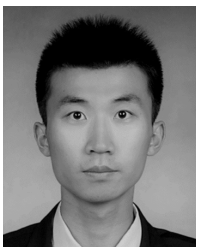

HE LIU was born in Jiamusi, China, in 1990. He received the B.Eng. degree in mechanical design manufacturing and automation and the M.Sc. degree in mechatronic engineering from the Harbin Institute of Technology, Harbin, China, in 2013 and 2015, respectively. He is currently pursuing the Ph.D. degree in mechanical engineering with the Mechatronics in Medicine Laboratory, Imperial College London, U.K.

FERDINANDO RODRIGUEZ Y. BAENA (Member, IEEE) received the M.Eng. degree in mechatronics and manufacturing systems engineering from King's College London, U.K., in 2000, and the Ph.D. degree in medical robotics from Imperial College London, in 2004. He is currently a Professor of medical robotics with the Department of Mechanical Engineering, Imperial College London, where he leads the Mechatronics in Medicine Laboratory. His research interests include mechatronic systems for diagnostics, surgical training, and surgical intervention.